# R-curve evaluation of 3YTZP/graphene composites by indirect compliance method

C. López-Pernía [a,b,*], C. Muñoz-Ferreiro [a,b,c], J. Prada-Rodrigo [d], P. Moreno [d], H. Reveron [c], J. Chevalier [c], A. Morales-Rodríguez [a], R. Poyato [a,b], Á. Gallardo-López [a]

[a] Universidad de Sevilla-ICMS (CSIC), Departamento de Física de la Materia Condensada, Apdo. 1065, 41080 Sevilla, Spain
[b] CSIC-Univ. de Sevilla, Instituto de Ciencia de Materiales de Sevilla (ICMS), Avda. Américo Vespucio 49, 41092 Sevilla, Spain
[c] Université de Lyon, INSA Lyon, MATEIS UMR CNRS 5510, 7 Avenue Jean Chapelle, F-69621 Villeurbane Cedex, France
[d] Grupo de Investigación en Aplicaciones del Láser y Fotónica (ALF-USAL), Universidad de Salamanca, Plaza de la Merced s/n, 37008 Salamanca, Spain

## ABSTRACT

This work addresses the crack growth resistance of 3 mol% Yttria-doped Tetragonal Zirconia Polycrystalline (3YTZP) spark-plasma sintered (SPS) composites containing two types of graphene-based nanomaterials (GBN): exfoliated graphene nanoplatelets (e-GNP) and reduced graphene oxide (rGO). The crack growth resistance of the composites is assessed by means of their R-Curve behavior determined by three-point bending tests on single edge "V" notched beams (SEVNB), in two different orientations of the samples: with the crack path perpendicular or parallel to the pressure axis during the SPS sintering. The sharp edge notches were machined by ultrashort laser pulsed ablation (UPLA). The compliance and optical-based methods for evaluating the crack length are compared on the basis of the experimental R-Curve results in composites with 2.5 vol% rGO tested in the perpendicular orientation. Moreover, the activation of reinforcement mechanisms is evaluated by both the fracture surface inspection by Scanning Electron Microscopy and a compliance analysis. It is shown that the indirect compliance method is relevant and reliable for calculating the R-Curve of 3YTZP/GBN composites. The effect of the type and content of GBN on the crack growth resistance of the composites is also discussed.

## 1. Introduction

Recently, Graphene-Based Nanomaterials (GBN), such as Graphene Nano-Platelets (GNP) or Reduced Graphene Oxide (rGO), have attracted a considerable scientific interest due to their potential to improve the mechanical properties of ceramic composites. In 2011, Walker et al. reported of 235% enhancement in the fracture toughness ($K_{IC}$) of $Si_3N_4$ ceramics when incorporating 1.5 vol% GNP [1]. Since then, many studies on the fracture toughness of several ceramic matrix composites containing graphene-based materials or carbon nanotubes have been carried out [1–8]. However, the results obtained up to date vary strongly with different parameters such as the type of GBN used as a filler, its content and its distribution throughout the ceramic matrix or the method employed for the fracture toughness determination. A good overview of the influence of the type and content of the GBN incorporated in ceramics is given by Miranzo el al. [3], making special emphasis on their mechanical, elastic and wear properties. Despite the variability of the results in the literature, the relative enhancement of $K_{IC}$ of the

composites when compared to the monolithic ceramic matrices has been reported to be higher for rGO as filler than for GNP. Moreover, the reinforcement effect is generally achieved for lower rGO contents than for GNP. The processing of ceramic/GBN composites is a crucial step in developing increased mechanical performance. If not optimized, adding GBN materials to the ceramic could be rather detrimental.

Another key aspect explaining the variability of the $K_{IC}$ values reported in the literature is the method to determine $K_{IC}$. The indentation method (IM) is one of the most frequently used due to its simplicity [9, 10]. It consists in the indirect determination of $K_{IC}$ from the direct measurement of the length of cracks emerging from the corners of Vickers indentation prints. However, the validity of the indentation method in ceramic/GBN composites is strongly questioned since the fracture toughness is estimated from a small region of the sample which is subjected to very complex stress fields [11–14]. Moreover, the microstructural anisotropy associated with these types of composites could lead to the absence of cracks in some directions of the sample, hampering the correct determination of $K_{IC}$ [4,15]. Other methods like

---

three- and four-point bending tests of single-edge notched beams (SENB) allow measuring toughness of these materials with better reliability [11]. However, the fracture toughness measured from these methods is strongly limited by a critical notch root radius [16]. Above it, the calculated $K_{IC}$ could be higher than the true fracture toughness of the material. Thus, the root radius of the notch should be sharp enough to obtain reliable $K_{IC}$ results. Similar to SENB, the Single-edge V-notched beams (SEVNB) consisted on the rectangular bars whose notch is machined with a saw cut. Then the notch tip is machined in "V" by using a razor blade with a diamond suspension. More recently, it has been reported that the razor blade can be replaced by machining a shallow sharp notch by ultra-short pulse laser ablation (UPLA)[17].

In most of the studies, the mechanical reinforcement of GBN/ceramic composites has been associated with energy dissipating mechanisms originated by GBN that hinder crack propagation. The most reported mechanisms are GBN pull-out and crack deflection, branching and bridging. Despite the undeniable influence of those mechanisms on the fracture resistance of these composites, detailed studies dedicated to the crack propagation behavior are very scarce, especially in relation to zirconia-based ceramic matrix composites [6,18,19]. In transformation toughened ceramics like yttria-stabilized tetragonal zirconia polycrystals (YTZP), the tetragonal to monoclinic phase transformation ability (mainly affected by the grain size of the ceramic matrix and the $Y_2O_3$ content), also contributes to the variability of reported fracture toughness values [20–23]. Moreover, in this type of composites, the reinforcement effect due to graphene is more difficult to assess.

Several ceramics show R-curve behavior which is characterized by an increase in crack growth resistance ($K_R$) with increasing crack length. The study of the R-curve of a given material allows the evaluation of its crack growth resistance since a rising R-curve is indicative of the development of toughening mechanisms. Despite the fact that most studies on GBN/ceramic composites report an increase in fracture toughness, there are only a few that examine their R-curve behavior [6, 16,17]. Moreover, most of them measure these properties only when the GBN main *a-b* plane is oriented perpendicular to the crack propagation path. In most GBN/ceramic composites the GBN tend to align perpendicularly to the compression force applied during sintering providing a structure similar to platelet-like or nacre-like materials. In a recent study, Liang et al. [24] addressed the excellent mechanical properties and the rising R-Curve of $Al_2O_3$ ceramics with highly oriented graphene nanolayers arranged in a nacre-like layer-by-layer structure. However, GBN/ceramic composites are highly anisotropic so questions about the influence of other orientations of GBN filler within the ceramic matrix do still arise. To the best of our knowledge only the work from Gómez-Gómez et al.[18] considered the R-curve behavior of the materials for two orientations of the sample.

For the R-curve determination, a test specimen with a crack is loaded in order to have a stable or controlled crack propagation. The main difference between various R-curve methods is the procedure for measuring the crack length during crack extension. The R-curve is often evaluated from load-displacement curves by crack lengths estimated indirectly by the compliance method which considers the increase in compliance of the material to calculate the crack length [25,26]. Although this method stands out for its simplicity, it may not be precise for materials with a strong R-curve, as the compliance could be affected by bridging stresses at the crack borders [27,28]. Thus, the real crack extension could be underestimated. In those cases, it becomes necessary to check its reliability by using other methods for a *direct* (optical) crack length determination. These methods may require the observation of the real crack length at the surface of the specimen with an optical microscope and even, the use of a video-recording unit for a closer study. *In-situ* measurements of the crack length during the mechanical test directly allow stress intensity factors calculation but they are difficult to set up, especially when considering nanostructured ceramics. Load-unload displacement tests could be also implemented to measure the crack length extension at different loads, by using optical or

scanning electron microscopes.

To get a better understanding of the mechanical behavior of zirconia ceramic/GBN composites, this work is conducted with the following objectives: (i) to validate the indirect compliance method for the R-curve calculation in zirconia/GBN composites, by comparing the results with the direct optical measurement of crack extension and (ii) to evaluate the influence of the incorporation of two different GBN materials (exfoliated Graphene Nano-Platelets (e-GNP) and reduced Graphene Oxide (rGO)) and their orientation on crack growth resistance of spark plasma sintered composites.

## 2. Experimental procedure

### 2.1. Materials preparation

#### 2.1.1. Powder processing and sintering

Commercial 3YTZP powder with 40 nm particle size (Tosoh Corporation, Tokyo, Japan) was annealed in order to remove organic additives [29] at 850 ℃ for 30 min in air before preparing the composite powders. GNP (ref. N006-P, lateral dimension < 5 μm and 10–20 nm thickness) and GO (ref. N002-PDE, lateral dimension ~ 7 μm and 2–3 nm thickness) powders were acquired from Angstrom Materials (Dayton, Ohio, USA) and used to prepare 3YTPZ-based composites.

Composite powders containing 2.5, 5 and 10 vol% of exfoliated GNP (e-GNP) were prepared using a planetary ball mill (Pulverisette 7, Fritsch, Germany) in dry conditions as described in [30]. Approximately 4 g of the GNP and 3YTZP powders were placed in a 45 mL zirconia jar together with seven 15 mm-diameter $ZrO_2$ balls. The powders were milled for 4 h at 350 rpm. Finally, composite powders were homogenized in an agate mortar.

Composite powders containing 2.5 vol% GO were prepared using a procedure that involves the combination of ultrasonic dispersion and high energy planetary ball-milling as described in [31]. First, the GO was dispersed in ethanol using a KT-600 ultrasonic probe (Kontes Inc., Vineland, NJ) at 20 kHz and 95% amplitude for 15 min, in time intervals of 5 min to avoid the heating of the suspension. Then, the 3YTZP powder was added to the GO suspension and sonicated for an additional 5 min. Then, the suspension was milled in the planetary ball mill in wet conditions during a short time (15 min) and at slow speed (250 rpm) to avoid damage of the GO layers. Finally, the powders were dried in a rotary evaporator and homogenized in an agate mortar. Pure 3YTZP reference ceramics were prepared from the 3YTZP powder after the annealing treatment.

All composite and pure 3YTZP powders were consolidated by Spark Plasma Sintering (SPS Model HP D25, FCT System GmbH, Germany) in vacuum atmosphere at 1250 ℃ for 5 min with an applied uniaxial pressure of 75 MPa. Disc samples (30 or 40 mm diameter and ~4 mm thick) were obtained. The GO reduction during SPS directly produces rGO-like fillers.

#### 2.1.2. SEVNB specimen preparation

The R-curve behavior of the composites and the 3YTZP benchmark was assessed on single-edge V notched beams (SEVNB). From each sintered disc, rectangular bars of size $25 \times 4 \times 3$ mm$^3$ (*L* x *W* x *B* with *L*=length, *W*=width and *B*=thickness) were cut and machined in accordance with the ASTM C1421–10 standard test method. A pre-notch of 2 mm depth was performed mechanically on the $25 \times 3$ mm$^2$ face with a diamond coated saw of 0.3 mm thick. In order to use a sharp notch that will ensure starting at lower $K_I$ and thus, obtain a more precise R-Curve[32,33], ultrashort pulsed laser ablation (UPLA) was used to produce an additional sharp notch of ~ 100 μm depth at the tip of the pre-notch with almost negligible thermal load on the substrate out of the ablated zone [17,18,34]. The laser notch was produced by a Ti: Sapphire system (Tsunami, Spectra Physics, USA) delivering pulses of duration 120 fs at λ = 795 nm with pulse energy 34 μJ and a repetition rate of 1 kHz. The full notch length ($a_0$) was estimated as the addition of

the pre-notch and the laser notch. A ratio $a_0/W \sim 0.5$ was achieved for all the specimens. An example of the sharp notch tip is shown in Fig. 1a.

In order to evaluate the effect of a possible GBN main plane preferential orientation with respect to the SPS pressing z-axis that would affect the crack resistance behavior of these materials, the tests were performed on samples in which the notch was performed on the surface perpendicular ($^\perp$) or parallel ($^{\parallel}$) to the SPS pressure z-axis. The test configuration is schematically shown in Fig. 1b and c, taking as an example the composite containing 2.5 vol% rGO. In the perpendicular configuration the main a-b plane of the rGO sheets is perpendicular to the crack plane. In the parallel configuration the crack path faces the edges of the rGO sheets.

Six SEVNB specimens for each type of composite were prepared. Three of them were prepared in order to be tested in the perpendicular ($^\perp$) configuration and the other three in the parallel ($^{\parallel}$) one. Hereinafter composite samples are labeled according to the type of GBN, its content and the tested configuration as $xGBN^\perp$ or $xGBN^{\parallel}$ (being "x" the GBN content). Finally, three SEVNB specimens of 3YTZP were tested in parallel ($^{\parallel}$) configuration and labeled 3YTZP.

## 2.2. Materials characterization

The densities of the sintered composites were measured using the Archimedes' method, with distilled water as the immersion medium. The theoretical densities were calculated based on the rule of mixtures considering densities of 6.05 g/cm$^3$ for 3YTZP and 2.2 g/cm$^3$ for GNP and rGO.

The semi-quantitative analysis of the crystallographic phases present in the sintered composites and the reference monolithic 3YTZP sample was carried out by X-Ray Diffraction (D8 Advanced A25 X-Ray diffractometer, (Bruker Co Massachusetts, USA).

The GBN distribution in the 3YTZP matrix as well as the morphology of the ceramic grains were characterized by Scanning Electron Microscopy (SEM) performed on fractured and polished cross-section surfaces (FEI Teneo, FEI, USA). Back-scattered electrons (BSE) mode was used for imaging GBN distribution throughout the ceramic matrix. To characterize zirconia grain sizes, polished surfaces were thermally etched in air at 1150 °C for 15 min in order to reveal the grain boundaries. The grain size was calculated as the equivalent planar diameter $d = 2(area/\pi)^{1/2}$ and the grain shape factor as $F = 4\pi area/(perimeter)^2$. More than 500 grains measurements were taking into account for each sample.

Raman spectroscopy was used to assess the presence and structural integrity of the GBN in the composites after the sintering process. In the composite containing 2.5 vol% rGO, the spectra were also acquired on the as-processed composite powders and compared to the ones obtained on sintered ceramics to account for the in-situ reduction of GO during the sintering process [31,35]. In order to characterize the transformability on 3YTZ and the composites, fractured surfaces are usually analyzed by XRD or Raman spectroscopy. In the present work, Raman spectroscopy was used to assess whether the t-m transformation took place on the SEVNB tested specimens [36]. Six to eight spectra from each specimen were acquired on fractured surfaces using a dispersive microscope (Horiba Jobin LabRam HR800, Kyoto, Japan) equipped with a He-Ne green laser (532.14 nm) at 20 mW. Since the t-phase may not transform homogeneously on the entire fracture surface [37], several spectra were acquired in different and random locations of the fracture surfaces.

The Young's modulus of all materials was measured at room temperature using a GrindoSonic equipment (MK6-A GrindoSonic BVBA Belgium), instrument based on the impulse excitation technique in which $25 \times 4 \times 3$ mm$^3$ samples were subjected to an initial deformation by means of a light mechanical impulse. Immediately, the object act as a spring-mass system and produce a transient mechanical vibration. The frequency of this vibration depends on the mass of the sample and its stiffness, which was determined following the ASTM E 1876–01 standard test method.

## 2.3. R-curve study

SEVNB specimens were tested in a three-point fixture (support span 21 mm) using an Instron 8500 machine (Norwood, USA). The support and upper cylinders were made of alumina and had a diameter of 8 mm. During the test, the specimen deflection was recorded using a Linear Variable Displacement Transducer (LVDT) placed near the sample notch. The R-Curves of the materials were built from the load-displacement ($P$-$\delta$) data obtained from the three-point bending tests according to two different methods. In most cases, R-Curves were obtained using the indirect compliance method [26]. In addition, and in order to validate this indirect method, the R-Curve of the composite with the highest crack resistance behavior ($2.5rGO^\perp$ composite) was also estimated from the direct measurement of crack growth by optical microscopy (load-unload three-point bending test).

### 2.3.1. R-curve determination by the indirect compliance method

The instantaneous applied load ($P_i$) and loading point displacement ($\delta_i$) data were recorded until the failure. The specimens were loaded in air with a constant low speed of 10 μm/min. The R-curve, showing the stress intensity factor ($K_{IR}$) as a function of the crack extension ($\Delta a = a_i - a_0$), was obtained by estimating the crack length and the stress intensity factor. For this, $K_{IR}$ was calculated by using the following expression:
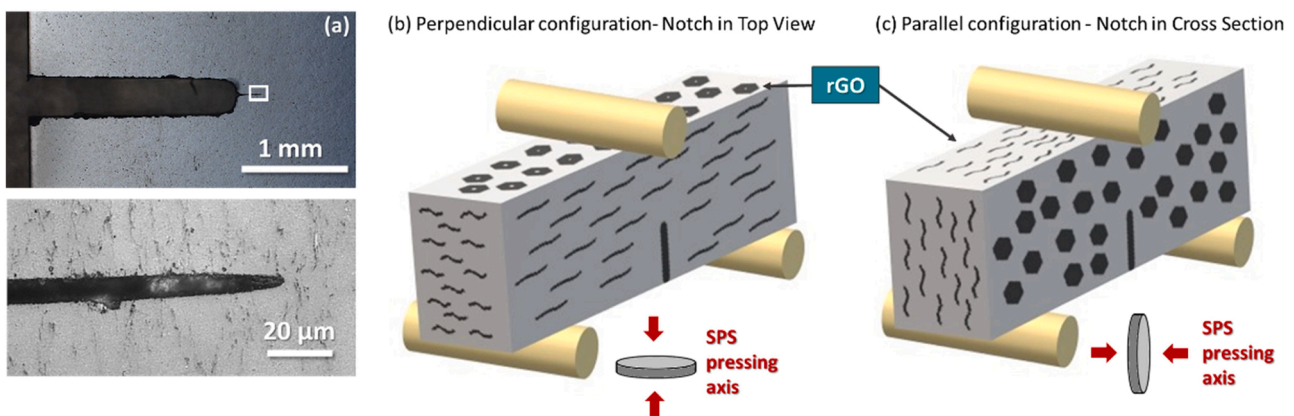


**Fig. 1.** (a) Optical images showing an example of the pre-notch (up) and the laser notch (down) performed on the samples. Schematics of the test configuration for the rGO samples. The notch is sawn in the surface (b) perpendicular or (c) parallel to the SPS pressing axis. The rGO sheets are "normal" or "edge-on", respectively, to the planar crack front.

$$K_{IR} = g \cdot \left[ \frac{P_i S_0}{B W^{3/2}} \right] \cdot \left[ \frac{3(a_i/W)^{1/2}}{2(1 - a_i/W)^{3/2}} \right] \tag{1}$$

where $P_i$ is the applied load, $S_0$ is the span, $B$ is the thickness of the sample, $W$ is the width of the sample, $a_i$ is the crack length and $g$ is a function depending on the geometry of the sample. The $g$ function was calculated according to ASTM C1421–10 standard test method [38].

An iterative method was used to calculate the instantaneous crack length ($a_i$) for each pair of experimental $P_i$- $\delta_i$ values as described by Munz and Fett [26]. First, the compliance ($C_i$) for each pair of data is defined as:

$$C_i = \frac{\delta_i}{P_i} \tag{2}$$

Then $a_i$ was estimated from the measured change in the compliance using the following equation:

$$a_i = a_{(i-1)} + \left[ \frac{W - a_{(i-1)}}{2} \cdot \frac{C_i - C_{(i-1)}}{C_i} \right] \tag{3}$$

### 2.3.2. Validation of the indirect compliance method

*2.3.2.1. R-curve determination by the optical method.* Direct R-curve determination consists on the optical measurement of the crack extension during the SEVNB test. Loading-unloading sequences on the SEVNB specimens were performed in air with a constant speed of 5 μm/min and load-displacement curves were recorded. $K_{IR}$ was still calculated using Eq. (1) with $P$ as the load at the maximum $\delta$ for each load-deflection curve. Here, the crack-length ($a_{opt}$) was measured directly by optical microscopy after each load-unload cycle to construct the R-curve which was compared with the one obtained by the indirect compliance method.

The compliance was calculated from the load-displacement point ($P$-$\delta$) according to Eq. (2) and its evolution as a function of the crack length, $C(a)$, was fitted to a linear function:

$$C(a) = Ma + N \tag{4}$$

This function was used to establish an empirical expression to estimate the crack length as a function of the measured changes in the compliance:

$$a = \frac{C - N}{M} \tag{5}$$

This expression was used to recalculate the R-curve obtained by the indirect compliance method in Section 2.3.1. This is, the corrected R-curve was built with $K_{IR}$ calculated from the load-displacement data of the first experiment according to Eq. (1) but substituting the crack length calculated from Eq. (5).

*2.3.2.2. Re-notching test and compliance analysis.* In order to simulate the propagation of a crack in an ideal material free of bridging or reinforcement mechanisms, a third study was performed. During this experiment, the notch length of the specimen tested was successively extended (re-notching) with a diamond coated saw. The re-notching operation was carried out after loading-unloading sequences, performed in air and at 5 μm/min. The applied load was stopped right before the crack could started to propagate, so no crack propagation was enhanced. The machined notch simulated a full crack without bridging and its length was measured after being sawn for each load-unload test by using optical microscopy. The compliance was calculated as the slope of the linear part of the $P$-$\delta$ curve obtained for each notch length. Based on this re-notching experiment, the compliance of re-notched sample was compared to the evolution of the compliance of the cracked specimen subjected to the test described in the previous section. This gave rise to an estimation of crack bridging stresses [39].

## 3. Results and discussion

### 3.1. Materials characterization

Well densified composites having relative densities $\geq$ 98.6% of the theoretical density (Table 1) were obtained after the SPS sintering process. The addition of GBN fillers slightly affected 3YTZP densification. The 3YTZP reference ceramic showed a relative density of 99.4% while it ranged from 99.4% to 97.9% (2.5% and 10 vol% e-GNP, respectively) and reached 98.6% in 2.5 vol% rGO composites. This slight decrease in density is in agreement with previously published studies [30,31,35].

The presence of the GBN phase in sintered composites was confirmed by Raman spectroscopy as the characteristic bands D, G and 2D located from ~1350 to ~2700 $cm^{-1}$ and related to graphitic materials were observed in all the Raman spectra (not shown here). We found that during the SPS process the GO phase was in-situ reduced to rGO, as confirmed by the variation in the intensity and width of D, G and 2D bands [31]. Moreover, regarding composites with e-GNP, we also corroborated the absence of GNP deterioration after the SPS process [30, 35].

The crystallographic phases present in monolithic 3YTZP and the as-sintered composites were checked by a semi-quantitative XRD analysis (not shown here). The only phase detected in all samples was the reduced tetragonal zirconia ($ZrO_{1.95}$). The reduction of the tetragonal phase is a consequence of the reducing conditions during the SPS since the powders are placed inside a graphite mold and the sintering process takes place under vacuum [30,31]. Although some authors have reported that the tetragonal to monoclinic zirconia phase transformation could be induced after sintering in graphene containing composites [29, 40], the main XRD monoclinic zirconia peaks located at $2\theta = 28.2$ y 31.4 ° were not observed in any of the samples prepared in the present work.

Fig. 2 shows the distribution of the graphene phase in the perpendicular to the SPS pressing axis cross-sections of the composites. Due to the different atomic number of the two main phases, they can be distinguished by BSE-SEM inspection since the dark phase will correspond to rGO or e-GNP while the clear one will be 3YTZP. A remarkable difference in the GBN size and distribution is observed in composites containing rGO compared to e-GNP. The rGO phase appears as large sheets with their main a-b plane aligned perpendicularly to the SPS pressing axis (Fig. 2a). In contrast, the e-GNP phase exhibits a smaller size (Fig. 2b to d) and the platelets are randomly distributed throughout the ceramic matrix, without any preferential orientation. This distribution features are observed in all e-GNP composites, independently of the amount of graphene.

Table 1 shows the estimated grain sizes in sintered, polished and thermal-etched surfaces. No grain refinement was observed in the composite containing 2.5 vol% rGO which exhibited a grain size similar to that of 3YTZP (0.24 and 0.23 μm, respectively). However, for composites containing e-GNP and independently of the content of graphene phase (i.e. 2.5–10 vol%), a slightly lower grain size ($\sim$ 0.18 μm) was obtained. Ceramic grain growth inhibition by graphene nanosheets has been previously linked to the fact that nanoplatelets surrounding ceramic grains act as diffusion barriers hindering the movement of the grain boundaries during sintering [41–43]. In 3Y-TZP/e-GNP

**Table 1**
Absolute and relative densities, grain size ($d_{planar}$) and elastic modulus (E) of the monolithic 3YTZP and the GBN/3YTZP composites.

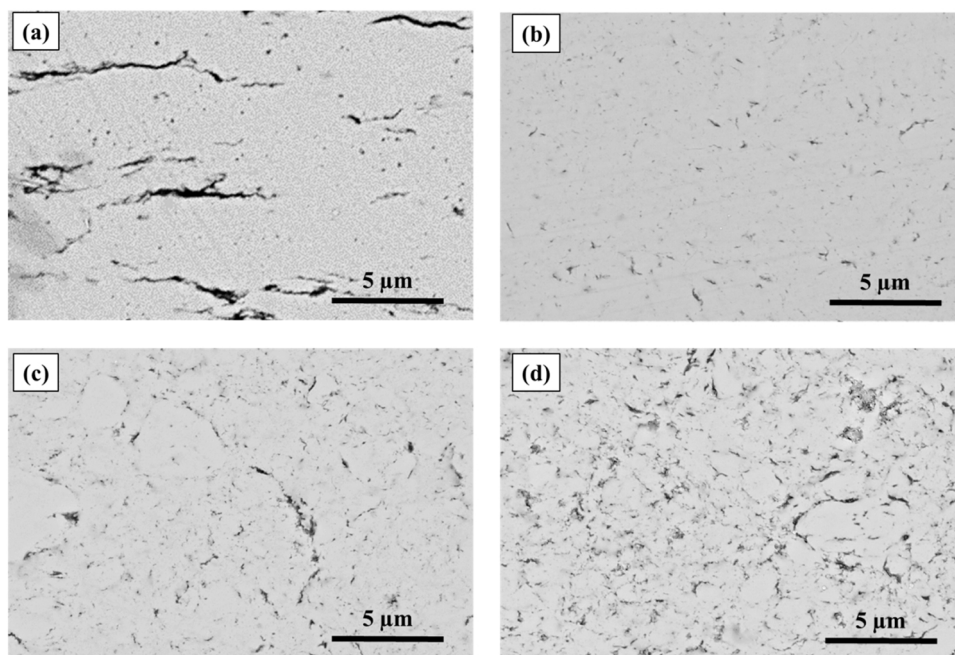| Samples | $\rho_{exp}$ (g/cm$^3$) | $\rho_{rel}$ (%) | $d_{planar} \pm$ s.d. (μm) | E (GPa) |
|---|---|---|---|---|
| 3YTZP | 6.01 ± 0.01 | 99.4 ± 0.1 | 0.23 ± 0.10 | 198 |
| 2.5 vol% rGO | 5.87 ± 0.04 | 98.6 ± 0.3 | 0.24 ± 0.13 | 185 |
| 2.5 vol% e-GNP | 5.93 ± 0.02 | 99.4 ± 0.2 | 0.18 ± 0.08 | 200 |
| 5 vol% e-GNP | 5.80 ± 0.01 | 98.7 ± 0.3 | 0.17 ± 0.07 | 191 |
| 10 vol% e-GNP | 5.58 ± 0.01 | 97.9 ± 0.2 | 0.18 ± 0.08 | 155 |

**Fig. 2.** BSE-SEM images from the cross sections perpendicularly to the SPS pressing axis of the sintered composites with (a) 2.5 vol% rGO, (b) 2.5 vol% e-GNP, (c) 5 vol% e-GNP and (d) 10 vol% e-GNP.
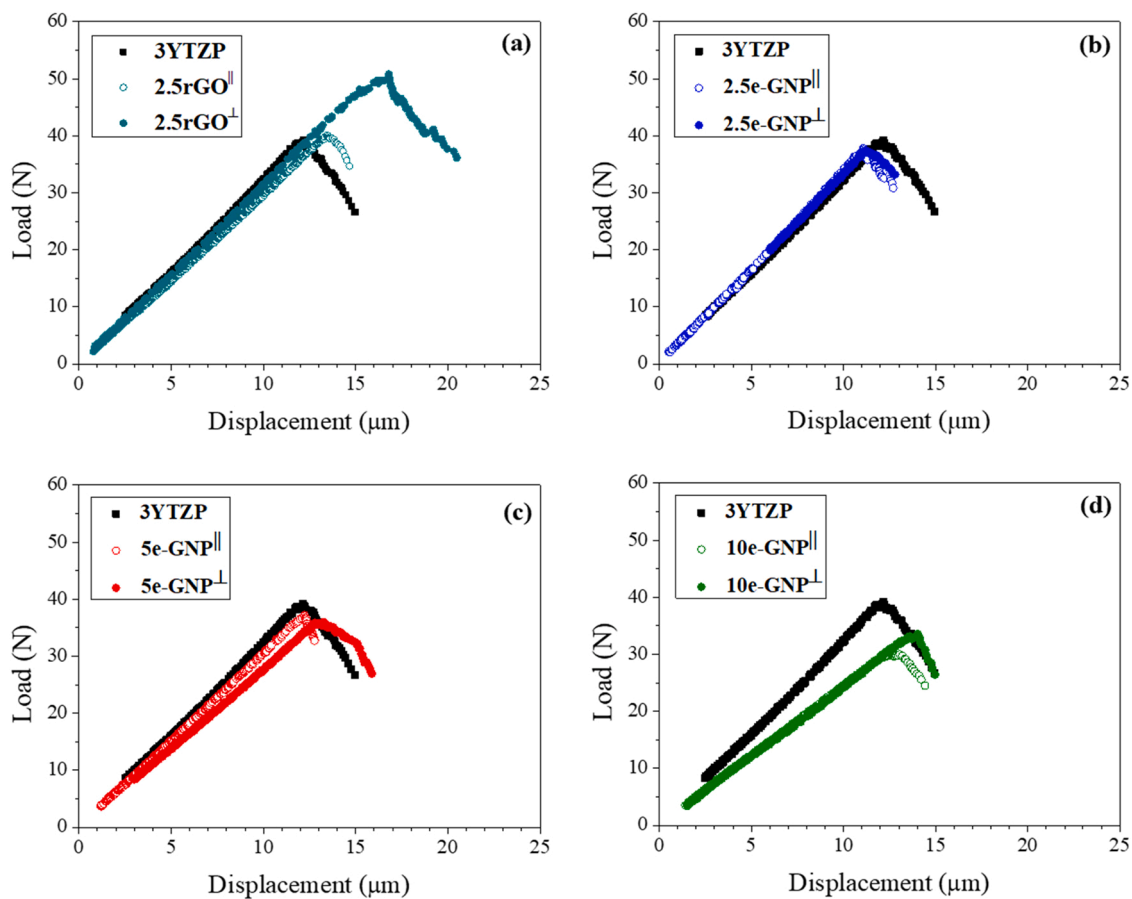


**Fig. 3.** Load-displacement curves under continuous loading at 10 μm/m for the monolithic 3YTZP and the composites containing (a) 2.5 vol% rGO, (b) 2.5 vol% e-GNP, (c) 5 vol% e-GNP and (d) 10 vol% e-GNP, in the parallel ($^{||}$) and perpendicular orientations ($^{\perp}$).

composites, the higher hindering effect may be associated with smaller (and therefore more numerous) graphene platelets which are more homogeneously distributed. Their small size was promoted by the use of the planetary ball milling under dry conditions [30]. Thus, there is a higher proportion of e-GNP surrounding a higher number of zirconia grains and hindering their growth.

A decrease in the elastic modulus (E) of 3YTZP-based composites after GBN addition was observed in 2.5 vol% rGO, 5 vol% e-GNP and 10 vol% e-GNP (Table 1). Moreover, E decreased as the e-GNP content increased. Although porosity can play a crucial role of decreasing the E of the composites, a similar densification degree was achieved for all the composites so this behavior can be related to the incorporation of more elastic graphene phases into the rigid ceramic matrix [4,44,45]. Despite of the high Young's modulus expected in a mechanically exfoliated monolayer of graphene (~ 1.0 TPa [46]), the elastic modulus of a monolayer of rGO is only ~ 0.25 TPa and it decreases about one order of magnitude in rGO consisting of more than 3 layers [47]. The elastic modulus of GNP is also considerably lower than the one of graphene [48]. This would therefore explain the decrease of E when incorporating the rGO and e-GNP in 3YTZP zirconia.

### 3.2. Effect of GBN addition on the crack resistance behavior of 3YTZP

Fig. 3 shows the three-point bending load-displacement curves of notched samples for zirconia (3YTZP) and 3YTZP composites (rGO and e-GNP) until fracture. Regarding 3YTZP/2.5 vol% rGO composites, the flexural deflection and maximum load achieved before fracture was higher in the perpendicular orientation ($\perp$) compared to the parallel orientation ($\parallel$) and the monolithic 3YTZP (Fig. 3a). On the other hand, the incorporation of e-GNP to the matrix had no significant effect in the load-displacement curves of 2.5 and 5 vol% e-GNP for the two tested orientations (Fig. 3a and b). Moreover, the maximum load before failure

decreased in 3YTZP/10 vol% e-GNP composites (both directions, Fig. 3d).

Related R-curves of composites and monolithic 3YTZP calculated by the compliance method are displayed in Fig. 4. It can be noticed that monolithic 3YTZP presented a very weak R-curve. The initial stress intensity factor ($K_{IR0}$) necessary for the onset of stable crack growth was of ~3.3 MPa m$^{1/2}$ and it increased during crack extension up to a plateau value of ~ 3.6 MPa m$^{1/2}$. This $K_{IR0}$ value is very close to the one obtained by Eichler et al. [49] in 3YTZP ceramics having similar grain size. Such a weakly rising 3YTZP R-curve can be explained by the relatively small grain size which also influences the fracture toughness of Y-TZP materials [50,51]. In general, ceramic crack growth resistance increases with increasing grain size. In the case of zirconia-based ceramics, higher grain size means a stronger ability for stress-induced tetragonal to monoclinic phase transformation [50,52]. Due to the singular stress field near a crack tip, tetragonal zirconia grains can undergo a stress-induced martensitic transformation creating a transformation zone ahead of the crack tip. As the volume of monoclinic cell is higher than that of the tetragonal one, a volumetric expansion strain of about 4–5% occurs and compressive stresses are applied along the crack length. The compressive stresses lead to a shielding stress intensity factor which must be overcome during crack propagation, in other words, the applied stress intensity factor must be increased to maintain stable crack growth. Clearly, the low values of $K_{IR0}$ and of the plateau value are linked to the small grain size of the SPS-sintered 3YTZP. This would indicate a lower propensity to phase transformation toughening than 3YTZP sintered at higher temperature, under conventional processes, as discussed below.

The incorporation of 2.5 vol% rGO clearly modifies the fracture behavior of 3YTZP matrix (Fig. 4a). Higher crack resistance was achieved when the planar crack front was perpendicularly oriented to the rGO main a-b plane (Fig. 1a). Although this composite showed an initial $K_{IR0}$ value of ~3.2 MPa m$^{1/2}$ similar to that obtained in 3YTZP, the
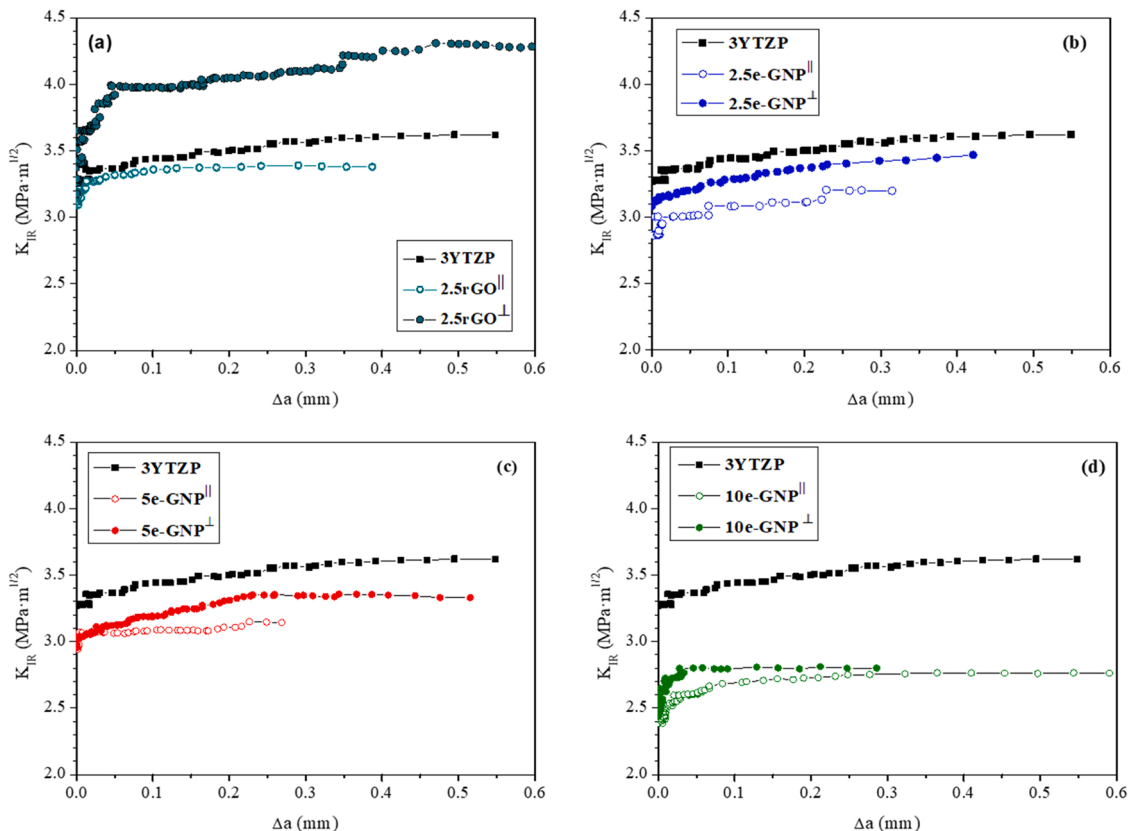


**Fig. 4.** R-Curves (stress intensity factor, $K_{IR}$, as a function of crack extension, $\Delta a$) obtained by the indirect compliance method for the monolithic 3YTZP and the composites containing (a) 2.5 vol% rGO, (b) 2.5 vol% e-GNP, (c) 5 vol% e-GNP and (d) 10 vol% e-GNP, in the parallel ($\parallel$) and perpendicular ($\perp$) orientations.

stress intensity factor increased up to ~ 4.3 MPa m$^{1/2}$. In the parallel orientation, the obtained R-curve was quite similar to that of monolithic 3YTZP (the stress intensity factor slightly increased from 3.1 MPa m$^{1/2}$ to 3.4 MPa m$^{1/2}$). This anisotropic R-curve behavior is in good agreement with microstructural features observed by BSE-SEM in this composite (Fig. 2a) since stronger reinforcement is expected when the crack front is running perpendicular to rGO plane.

The effect of incorporating e-GNP on the R-curve of the composites is quite different (Fig. 4a, b and c) and even was negative with respect to the mechanical behavior. For 2.5 and 5 vol% e-GNP, $K_{IR}$ values were slightly lower than those observed on monolithic zirconia. Although the microstructural observations did not reveal any preferential orientation of e-GNP, smaller differences between the two tested orientations could be related to some degree of anisotropy or preferential orientation of the platelets. Accordingly, in 2.5e-GNP and 5e-GNP composites $K_{IR}$ values increased softly up to ~3.4 MPa m$^{1/2}$ when tested in the perpendicular configuration while they only reached 3.1 MPa m$^{1/2}$ in the parallel configuration. When increasing the content of e-GNP up to 10 vol%, the crack growth resistance remarkably decreased compared to that of the composites with 2.5 and 5 vol% e-GNP and the monolithic 3YTZP. Moreover, microstructural anisotropy is probably minor as the steady-state $K_{IR}$ values were similar for the two configurations (~2.8 MPa m$^{1/2}$). In addition, unlike the behavior observed in monolithic 3YTZP and composites with a lower e-GNP content, the R-curve of 10e-GNP$^{\perp}$ rose abruptly from the start of crack extension (Fig. 4d), recalling the behavior already discussed for 2.5rGO$^{\perp}$ (Fig. 4a).

To assess the effect of the graphene phase on the R-curve behavior of the composites, three factors should be considered. The first one is the effect of the stress-induced tetragonal to monoclinic (t-m) zirconia phase transformation at the crack tip, the second one is the effect of the grain size and the last one is the interaction of the GBN filler with the crack propagation (bridging effects).

### 3.2.1. Stress-induced t-m phase transformation and zirconia grain size effect

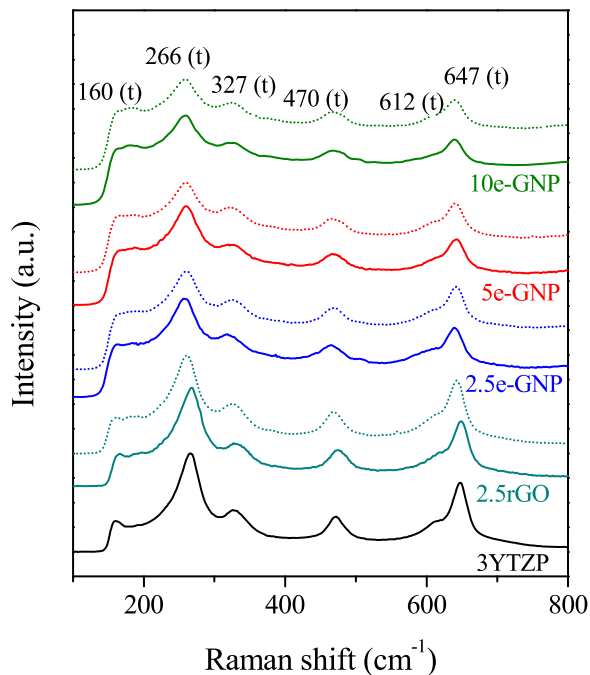Fig. 5 shows the Raman spectra acquired on the fractured surfaces of



**Fig. 5.** Evaluation of the tetragonal phase by Raman spectroscopy in the fracture surface of the composites and the monolithic 3YTZP. Dotted and solid lines correspond to the specimens tested in the parallel ($^{||}$) and perpendicular ($^{\perp}$) configuration, respectively.

monolithic 3YTZP and composites, in the range where the main tetragonal and monoclinic zirconia peaks appeared (100–800 cm$^{-1}$). The six theoretically predicted Raman peaks for tetragonal zirconia [36,53] at 160, 266, 327, 470, 612 and 647 cm$^{-1}$ were clearly detected in all the fractured surfaces while the two monoclinic main peaks expected to appear at 178 and 189 cm$^{-1}$ were not observed. The absence of monoclinic peaks suggests a null or very weak t-m transformation during crack propagation. This lack of phase transformation is related to the fine zirconia grain size developed by SPS [50,54]. It is also consistent with the low values of $K_{IR0}$. Therefore, the crack resistance behavior of the SPS sintered composites developed in this work is mainly expected to be driven by the graphene fillers.

### 3.2.2. Fracture mechanisms influenced by GBN fillers

Fracture surfaces features after the SEVNB tests revealed a combination of inter- and intragranular fracture in all the investigated materials (Fig. S1 in the Supplementary Section). However, the strongly intergranular fracture mode observed in 3YTZP/e-GNP composites may explain the lower $K_{IR}$ values, as grain boundaries are areas mechanically weaker than gains where cracks can easily propagate [55]. In addition, as the lateral size of the GBN in as-prepared composites was notably small, they probably did not provide significant reinforcement to the 3YTZP matrix.

Fractured surfaces of composites containing e-GNP are shown in Figs. 6 and 7 and S1. The flatter geometry and the smaller size of the e-GNP compared to rGO is clearly noticed, corroborating what was previously stated in the BSE-SEM images of the Fig. 2. The fracture surface roughness increases with the e-GNP content (Fig. 6). Thus, although the obtained R-curve behavior seems to be similar to that of 3YTZP, the slightly lower $K_{IR}$ values could be related to e-GNP that can act as flaws or defects favoring crack propagation. When increasing the e-GNP content, the amount of nanostructures acting as flaws increases, so a decrease of the fracture resistance would be expected, as observed. However, the composite with 2.5 vol% e-GNP presents a similar R-curve to the one with 5 vol% e-GNP, in both orientations (Fig. 4b and c). The examination of the fracture surfaces of the 5e-GNP$^{\perp}$ and the 5e-GNP$^{||}$ specimens show some features that could be related to some toughening mechanisms. Several spherical-shaped voids or craters can be found throughout the whole fracture surface indicating a lower energy path for crack deflection (Figs. 6b and 7a to c). These features can be clearly found in both orientations of the composite and also for 10 vol% e-GNP. A close SEM examination suggests that the e-GNP are firmly bonded to the zirconia grains (Fig. 7d), which could induce the crack to seek a lower energy path and deflect. It is, in this case, along the e-GNP-zirconia interfaces. The spherical shape of these paths is not related to pores but to the distribution of the e-GNP throughout the ceramic matrix since the e-GNP seem to be surrounding some regions of zirconia (Fig. 2). These regions may be related to the presence of some zirconia agglomerates formed during the powder processing step. As it can be observed in Fig. 7c, the interface between the e-GNP and the zirconia may be the most favorable path for the crack to propagate. The crack propagates along the weak e-GNP-zirconia boundaries creating a tortuous path and a rougher surface than monolithic 3YTZP. To the best of our knowledge, this is the first time that the spherical deflection of the cracks is observed on ceramic matrix composites. Although the microscopic observations also reveal the occurrence of the pulling out of the e-GNP (Fig. 7d), the size of the e-GNP is not enough to provide crack bridging. In Fig. 7c the branching of the crack can also be observed, however the energy dissipation of these mechanisms is comparatively lower than the contribution of bridging to the toughening. Thus, lower crack resistance than monolithic 3YTZP are obtained for these composites. These results are in good agreement with previous works [12, 56] that reported that the GNP present a high resistance to be pulled out contributing to the dissipation of energy associated with crack propagation by creating a more tortuous path.

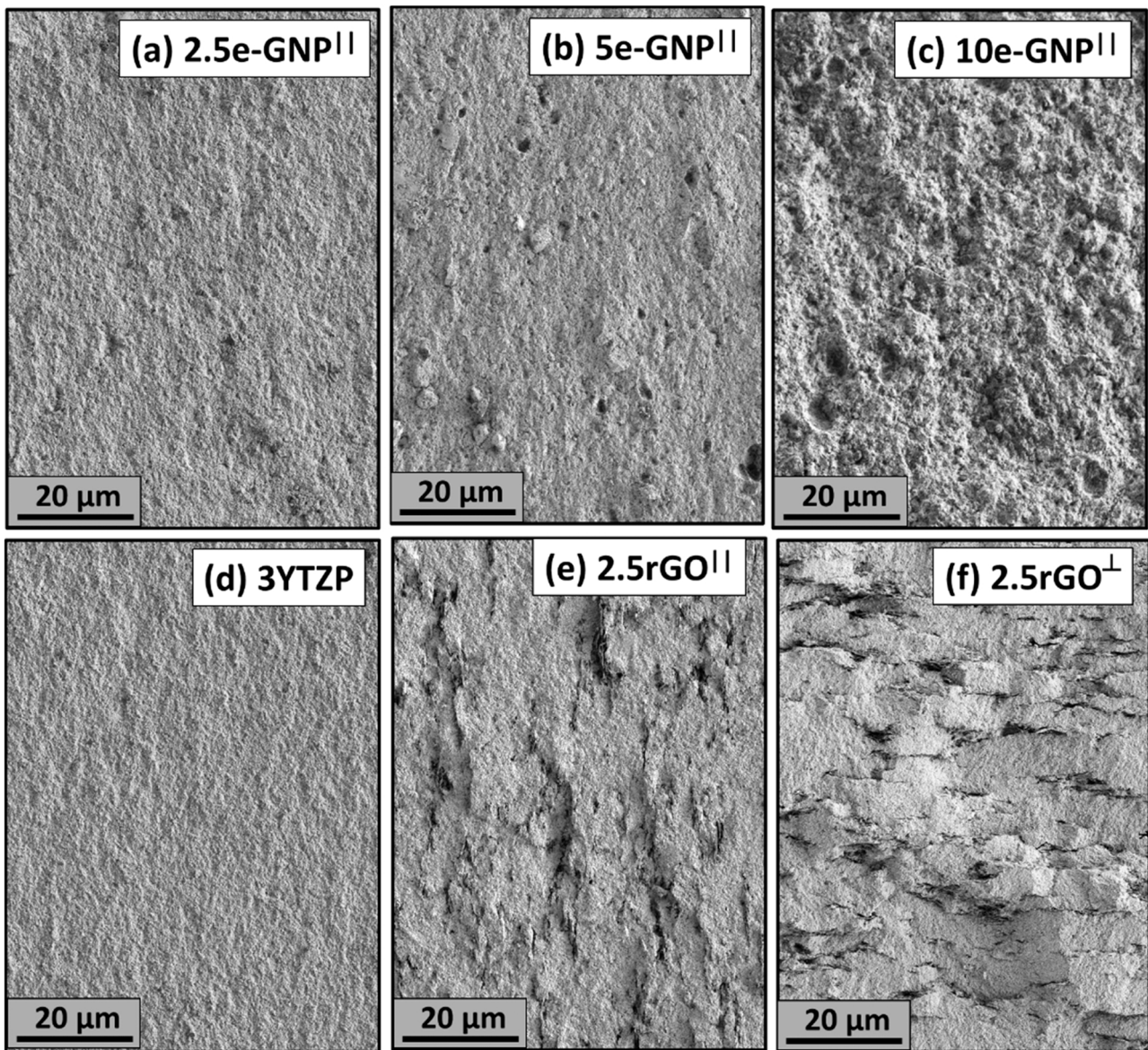For the composite with 10 vol% e-GNP, the presence of these

Fig. 6. Fracture surfaces of the monolithic 3YTZP and the composites.

spherical voids is increased leading to a very rough fracture surface (Fig. 6c). This slightly increase in the crack tortuosity suggests that a certain small propagation inhibition effect was exerted by e-GNP. Moreover, crack deflection is also evidence in Fig. 7e, as shown by the abrupt change in crack direction. However, the low $K_{IR}$ values obtained for this composite suggest that the effect of these mechanisms for energy dissipation is counterbalanced by the presence of more e-GNP that favor the crack propagation [12]. As in the composites with lower content of GNP, the crack propagation takes place along the GBN-zirconia interfaces, which gives a tortuous path and a rougher surface than monolithic 3YTZP but a lower crack resistance overall. This would explain also why, despite the very low $K_{IR}$ values of this composite, its R-curve rose very steeply at the beginning, for low crack displacements (Fig. 4d).

Further SEM examination of the fractured specimens reveals that the rGO layers interact with the propagating cracks providing different mechanisms to enhance the fracture resistance of the material in the perpendicular orientation. Figs. 6f and 8 shows the fracture surface of the 2.5rGO$^\perp$ composite. The preferential orientation of the rGO sheets, with their a-b main plane perpendicular to the SPS pressing axis is clearly observed. Figs. 6f and 8 are clear examples of the multiple

toughening events occurring as the crack propagates. The phenomena of crack branching as experienced during crack propagation is highlighted in Fig. 8a. Figs. 6f and 8b evidences the deflection of the crack when it encounters the graphene plane. The fact that several protruded rGO sheets are noticed on the fracture surface suggests the pulling out of the rGO sheets, which indicate the potential of crack bridging being involved. It is likely that crack bridging is the main source of toughening for the 2.5rGO$^\perp$ composite. The rGO sheets also show an undulation shape that has been also proposed as a potential reinforcement mechanism [57]. These observations would explain the strong R-curve and the high $K_{IR}$ plateau value obtained for this composite. The effect of the rGO layers on the enhancement of the crack resistance behavior is significant only when their main a-b plane is perpendicularly oriented to the planar crack front. Fig. 6e shows that the deflection of the crack significantly decreases when the crack front is facing the rGO layer edges (parallel orientation). According to Gómez-Gómez et al.[18], the reason for this behavior is the lower "effective" area of graphene material intersecting the crack front compared to what happens when the crack faces the a-b plane of rGO.
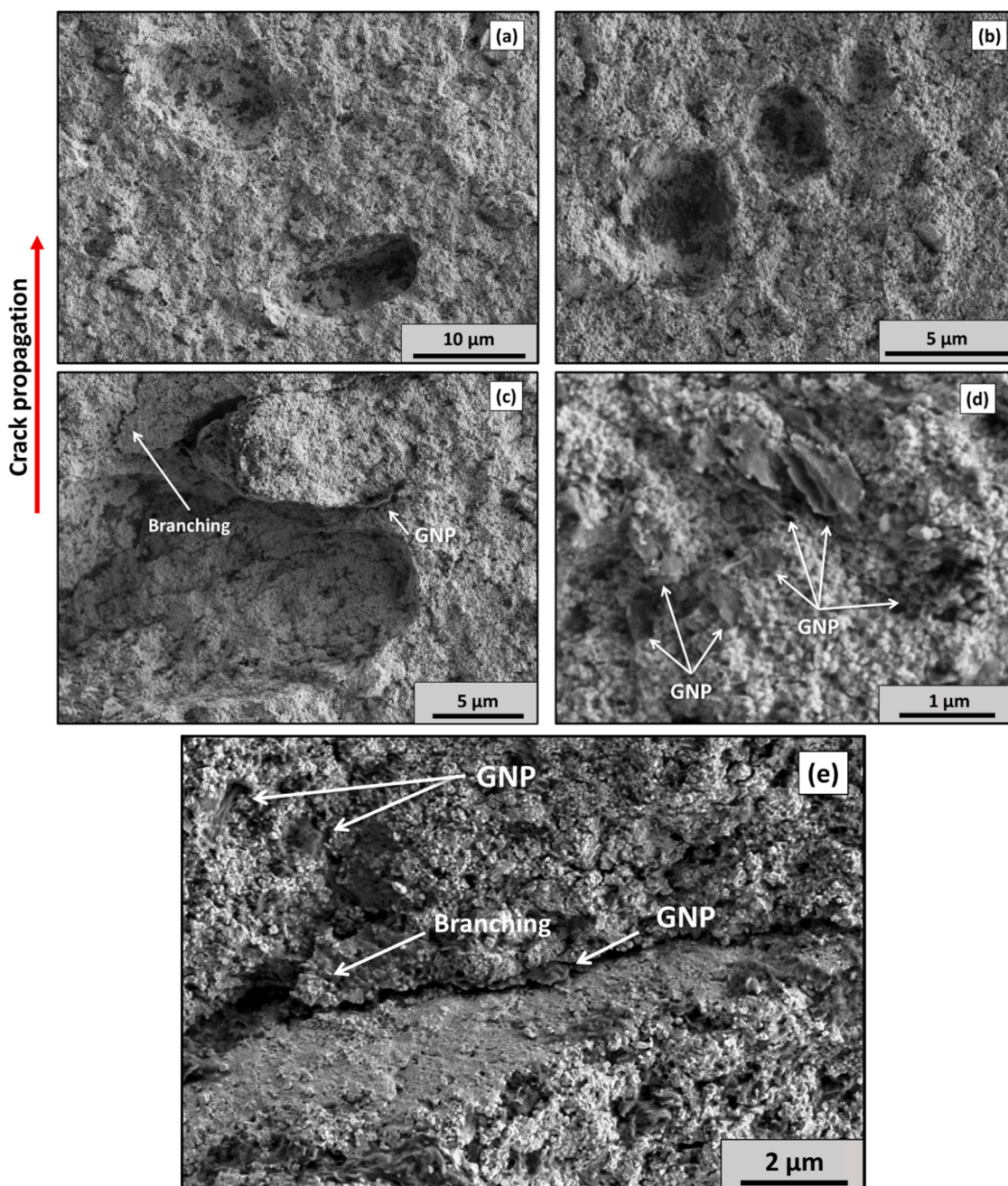
**Fig. 7.** Spherical features found in both (a) perpendicular and (b) parallel orientations of the composite with 5 vol% e-GNP. (Compression axis during SPS is indicated by yellow arrows). Fracture surfaces revealing the toughening mechanisms found in the composites with 5 vol% e-GNP: (c) crack deflection and branching and (d) e-GNP pull-outs. (e) Toughening mechanisms found in the perpendicular composite with 10 vol% e-GNP.

### 3.3. Validation of the R-curve determination by the indirect compliance method

As it can be noted in Fig. 4, the addition of a 2.5 vol% rGO clearly modifies the fracture behavior of monolithic 3YTZP in the perpendicular configuration. It is the strongest R-curve behavior developed in this work, with the highest $K_{IR}$ improvement with crack extension and the only one with a higher plateau compared to that of the monolithic 3YTZP. For this reason, the validation of the compliance method in obtaining the R-curve of 2.5rGO$^\perp$ composite was assessed. Let us recall here that the compliance method can underestimate the real crack length if large bridging interactions operate during the crack propagation, in particular for large crack extensions[58]. This behavior is related to bridging effects because a partially bridged crack with unbroken ligaments leads to a higher stiffness of the cracked specimen than a crack without bridging interactions.

Fig. 9a shows the R-curve obtained by the direct optical measurement of the real crack length on a side surface of the 2.5rGO$^\perp$ test specimen (blue/black circles). The R-curve obtained by the compliance method (green circles) is also included for comparison as well as the corrected one (empty circles). The evolution of the compliance ($C$) with the real crack length fitted to a linear function according to Eq. (2) is shown in Fig. 9b. The obtained parameter $B$ (slope) in this fitting was $B_{real\ crack} = (4.0 \pm 0.3) \times 10^{-4} \, N^{-1}$. Based on this fitting, the crack length calculated by the compliance method was corrected and thus, the R-curve obtained by the indirect compliance method. The compliance calculated in a set of samples with artificial crack lengths imposed by successively re-notching of the 2.5rGO$^\perp$ composite is also shown in
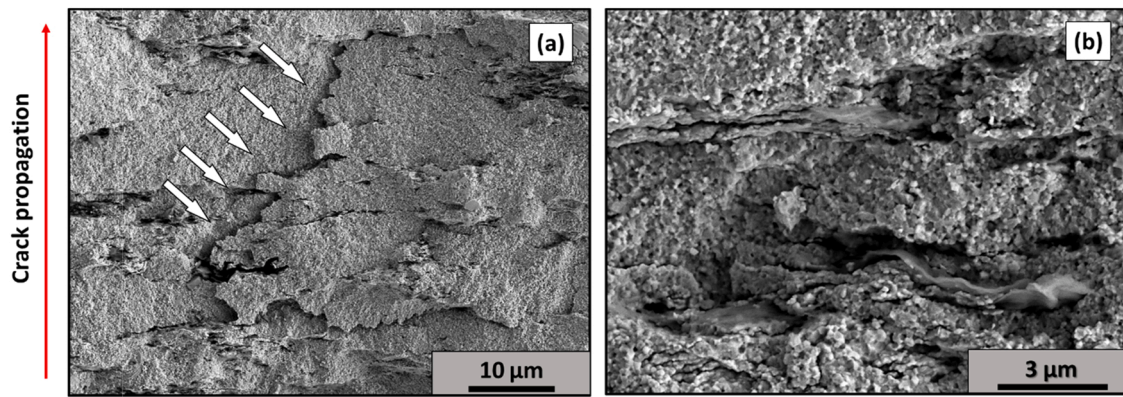
**Fig. 8.** Fracture surfaces of the composites with 2.5 vol%. rGO tested in the perpendicular orientations. Fracture surfaces revealing the toughening mechanisms found in this composite: (a) crack branching (indicated with arrows), (b) rGO pull-out and crack deflection.
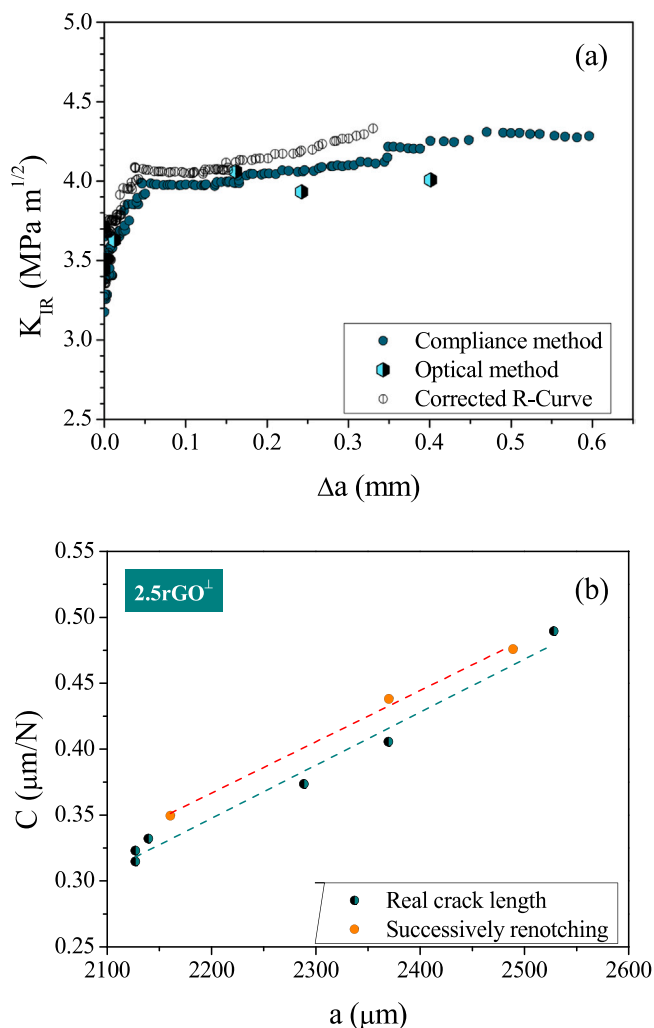


**Fig. 9.** (a) R-Curves from the 2.5rGO$^{\perp}$ composite obtained by the optical method (blue/black circles), the compliance method (green circles) and recalculating the crack length used in the compliance method (empty circles). (b) Evolution of the compliance ($C$) with the real crack extension ($a$) and the successively renotching of the samples.

Fig. 9b.

It is clearly noted in Fig. 9a that R-curves obtained by the different methods are very similar. In the R-Curve obtained with crack lengths measured by the optical method, the initial $K_{I0}$ was 3.4 MPa m$^{1/2}$ and

increased up to a steady-state stress intensity factor of $\sim$ 4.0 MPa m$^{1/2}$, while in the corrected compliance method the $K_{IR}$ plateau value was reached at $\sim$ 4.2 MPa m$^{1/2}$. These values did not even differ from the $K_{IR}$ plateau value ($\sim$ 4.3 MPa m$^{1/2}$) of the R-Curve obtained by the compliance method (Fig. 4a). It can be concluded that the compliance method provides an accurate evaluation R-curve behavior of these materials.

The re-notching study was carried out to further assess the presence of strong bridging mechanisms that affect the R-curve of the composites. The evolution of the compliance ($C$) with the real notch extension was compared to the evolution of the compliance with the real crack extension in the same type of composites (Fig. 9b). According to Eq. (2), the parameter $B$ (slope) obtained from the relation of the compliance with the notch length is $B_{renotching} = (3.9 \pm 0.3)$ x10$^{-4}$ N$^{-1}$. This slope is the same as that obtained for the real crack extension, which confirms the validation of the compliance method to accurately describe the crack length evolution from the compliance measured. The intercept is slightly higher for the re-notched samples than for the cracked samples, indicating that the reinforcing effect of the rGO phase by bridging is real but quite modest. This result validates the use of the simpler compliance method as a way to accurately obtain the R-curve of studied graphene-zirconia composites.

## 4. Conclusions

The simple, fast and easy tool for calculating R-curves from the indirect compliance method could be used accurately to characterize the here-developed zirconia-based graphene composites.

The absence of stress-induced t-m zirconia phase transformation, due to the small grain size developed by SPS, makes GBN interaction with the crack front the main mechanisms for improving crack resistance, crack bridging being likely the most important mechanism accounting for a potential R-Curve development. Further work could be interesting to combine stress-induced transformation toughening (for example by lowering the yttria content and/or increasing the grain size) to the mechanisms related to the presence of GBN.

The GBN features and content will determine the crack resistance behavior of 3YTZP. Their geometry, distribution and orientation in the ceramic matrix are the aspects that have the greatest impact on the propagation of crack. Therefore and because of its low lateral dimensions, no significant reinforcement effect was provided by the incorporation of e-GNP into the ceramic matrix. On the contrary, the addition of larger sheets of rGO modified the 3YTZP R-curve.

The composite showing the best crack propagation resistance contained 2.5 vol% rGO and was tested in a configuration in which the GBN main plane was oriented perpendicularly to the crack propagation path. An increase of the $K_{IR}$ plateau value of $\sim$20% compared to 3YTZP was achieved in this composite and attributed to mechanisms such as crack

deflection and branching, and rGO pull-out. No crack resistance enhancement was observed in the composites with e-GNP since the reinforcement effect provided by the energy dissipation mechanisms, such as the crack deflections through spherical-shaped voids, is counterbalanced by their small dimensions, which makes them act as flaws that favor crack propagation. We therefore strongly advise to measure R-Curve and evaluate toughness in all directions, and not only the 'good one' to give an overall figure of crack propagation behavior.

## Declaration of Competing Interest

The authors declare that they have no known competing financial interests or personal relationships that could have appeared to influence the work reported in this paper.

## Acknowledgments

## Appendix A. Supplementary material

Supplementary data associated with this article can be found in the online version at doi:10.1016/j.jeurceramsoc.2023.02.002.

## References

[1] L.S. Walker, V.R. Marotto, M.A. Rafiee, N. Koratkar, E.L. Corral, Toughening in graphene ceramic composites, ACS Nano 5 (2011) 3182–3190, https://doi.org/10.1021/nn200319d.

[2] J. Zhu, H.M. Wong, K.W.K. Yeung, S.C. Tjong, Spark plasma sintered hydroxyapatite/graphite nanosheet and hydroxyapatite/multiwalled carbon nanotube composites: mechanical and in vitro cellular properties, Adv. Eng. Mater. 13 (2011) 336–341, https://doi.org/10.1002/adem.201000300.

[3] P. Miranzo, M. Belmonte, M.I. Osendi, From bulk to cellular structures: a review on ceramic/graphene filler composites, J. Eur. Ceram. Soc. 37 (2017) 3649–3672, https://doi.org/10.1016/j.jeurceramsoc.2017.03.016.

[4] H. Porwal, P. Tatarko, S. Grasso, J. Khaliq, I. Dlouhý, M.J. Reece, Graphene reinforced alumina nano-composites, Carbon 64 (2013) 359–369, https://doi.org/10.1016/j.carbon.2013.07.086.

[5] K. Wang, Y. Wang, Z. Fan, J. Yan, T. Wei, Preparation of graphene nanosheet/alumina composites by spark plasma sintering, Mater. Res. Bull. 46 (2011) 315–318, https://doi.org/10.1016/j.materresbull.2010.11.005.

[6] A. Centeno, V.G. Rocha, B. Alonso, A. Fernández, C.F. Gutierrez-Gonzalez, R. Torrecillas, A. Zurutuza, Graphene for tough and electroconductive alumina ceramics, J. Eur. Ceram. Soc. 33 (2013) 3201–3210, https://doi.org/10.1016/j.jeurceramsoc.2013.07.007.

[7] P. Kun, O. Tapasztó, F. Wéber, C. Balázsi, Determination of structural and mechanical properties of multilayer graphene added silicon nitride-based composites, Ceram. Int. 38 (2012) 211–216, https://doi.org/10.1016/j.ceramint.2011.06.051.

[8] J. Dusza, J. Morgiel, A. Duszová, L. Kvetková, M. Nosko, P. Kun, C. Balázsi, Microstructure and fracture toughness of Si$_3$N$_4$ +graphene platelet composites, J. Eur. Ceram. Soc. 32 (2012) 3389–3397, https://doi.org/10.1016/j.jeurceramsoc.2012.04.022.

[9] A.G. Evans, E.A. Charles, Fracture toughness determinations by indentation, J. Am. Ceram. Soc. 59 (1976) 371–372, https://doi.org/10.1111/j.1151-2916.1976.tb10991.x.

[10] G.R. Anstis, P. Chantikul, B.R. Lawn, D.B. Marshall, A critical evaluation of indentation techniques for measuring fracture toughness: I, direct crack

[11] measurements, J. Am. Ceram. Soc. 64 (1981) 533–538, https://doi.org/10.1111/j.1151-2916.1981.tb10320.x.

[11] K. Markandan, J.K. Chin, M.T.T. Tan, Recent progress in graphene based ceramic composites: a review, J. Mater. Res. 32 (2017) 84–106, https://doi.org/10.1557/jmr.2016.390.

[12] I. Ahmad, M. Islam, H.S. Abdo, T. Subhani, K.A. Khalil, A.A. Almajid, B. Yazdani, Y. Zhu, Toughening mechanisms and mechanical properties of graphene nanosheet-reinforced alumina, Mater. Des. 88 (2015) 1234–1243, https://doi.org/10.1016/j.matdes.2015.09.125.

[13] G.D. Quinn, R.C. Bradt, On the Vickers indentation fracture toughness test, J. Am. Ceram. Soc. 90 (2007) 673–680, https://doi.org/10.1111/j.1551-2916.2006.01482.x.

[14] R. Morrell, Fracture toughness testing for advanced technical ceramics: internationally agreed good practice, Adv. Appl. Ceram. 105 (2006) 88–98, https://doi.org/10.1179/174367606X84422.

[15] N. Obradović, F. Kern, Properties of 3Y-TZP zirconia ceramics with graphene addition obtained by spark plasma sintering, Ceram. Int. 44 (2018) 16931–16936, https://doi.org/10.1016/j.ceramint.2018.06.133.

[16] R. Damani, R. Gstrein, R. Danzer, Critical notch-root radius effect in SENB-S fracture toughness testing, J. Eur. Ceram. Soc. 16 (1996) 695–702, https://doi.org/10.1016/0955-2219(95)00197-2.

[17] M. Turon-Vinas, M. Anglada, Fracture toughness of zirconia from a shallow notch produced by ultra-short pulsed laser ablation, J. Eur. Ceram. Soc. 34 (2014) 3865–3870, https://doi.org/10.1016/j.jeurceramsoc.2014.05.009.

[18] A. Gómez-Gómez, C. Ramírez, J. Llorente, A. Garcia, P. Moreno, H. Reveron, J. Chevalier, M.I. Osendi, M. Belmonte, P. Miranzo, Improved crack resistance and thermal conductivity of cubic zirconia containing graphene nanoplatelets, J. Eur. Ceram. Soc. 40 (2020) 1557–1565, https://doi.org/10.1016/j.jeurceramsoc.2019.12.016.

[19] O.T. Picot, V.G. Rocha, C. Ferraro, N. Ni, E. D'Elia, S. Meille, J. Chevalier, T. Saunders, T. Peijs, M.J. Reece, E. Saiz, Using graphene networks to build bioinspired self-monitoring ceramics, Nat. Commun. 8 (2017) 14425, https://doi.org/10.1038/ncomms14425.

[20] J.-H. Shin, S.-H. Hong, Fabrication and properties of reduced graphene oxide reinforced yttria-stabilized zirconia composite ceramics, J. Eur. Ceram. Soc. 34 (2014) 1297–1302, https://doi.org/10.1016/j.jeurceramsoc.2013.11.034.

[21] F. Chen, D. Jin, K. Tyeb, B. Wang, Y.H. Han, S. Kim, J.M. Schoenung, Q. Shen, L. Zhang, Field assisted sintering of graphene reinforced zirconia ceramics, Ceram. Int. 41 (2015) 6113–6116, https://doi.org/10.1016/j.ceramint.2014.12.147.

[22] S. Ramesh, M.M. Khan, H.C. Alexander Chee, Y.H. Wong, P. Ganesan, M.G. Kutty, U. Sutharsini, W.J.K. Chew, A. Niakan, Sintering behaviour and properties of graphene oxide-doped Y-TZP ceramics, Ceram. Int. 42 (2016) 17620–17625, https://doi.org/10.1016/j.ceramint.2016.08.077.

[23] S. Su, Y. Chen, Q. Huang, Graphene nanosheet-induced toughening of yttria-stabilized zirconia, Appl. Phys. A 123 (2017) 10, https://doi.org/10.1007/s00339-016-0613-7.

[24] L. Liang, C. Huang, C. Wang, X. Sun, M. Yang, S. Wang, Y. Cheng, Y. Ning, J. Li, W. Yin, Y. Li, Ultratough conductive graphene/alumina nanocomposites, Compos Part A Appl. Sci. Manuf. 156 (2022), 106871, https://doi.org/10.1016/j.compositesa.2022.106871.

[25] S. Fünfschilling, T. Fett, R. Oberacker, M.J. Hoffmann, H. Özcoban, H. Jelitto, G. A. Schneider, J.J. Kruzic, R curves from compliance and optical crack-length measurements, J. Am. Ceram. Soc. 93 (2010) 2814–2821, https://doi.org/10.1111/j.1551-2916.2010.03758.x.

[26] D. Munz, T. Fett, Ceramics, Springer Berlin Heidelberg, Berlin, Heidelberg, 1999, https://doi.org/10.1007/978-3-642-58407-7.

[27] T. Fett, Influence of bridging stresses on specimen compliances, Eng. Fract. Mech. 53 (1996) 363–370, https://doi.org/10.1016/0013-7944(95)00142-5.

[28] T. Fett, Determination of bridging stresses and R-curves from load-displacement curves, Eng. Fract. Mech. 52 (1995) 803–810, https://doi.org/10.1016/0013-7944(95)00053-X.

[29] A. Gallardo-López, I. Márquez-Abril, A. Morales-Rodríguez, A. Muñoz, R. Poyato, Dense graphene nanoplatelet/yttria tetragonal zirconia composites: Processing, hardness and electrical conductivity, Ceram. Int. 43 (2017) 11743–11752, https://doi.org/10.1016/j.ceramint.2017.06.007.

[30] C. López-Pernía, C. Muñoz-Ferreiro, C. González-Orellana, A. Morales-Rodríguez, Á. Gallardo-López, R. Poyato, Optimizing the homogenization technique for graphene nanoplatelet/yttria tetragonal zirconia composites: influence on the microstructure and the electrical conductivity, J. Alloy. Compd. 767 (2018) 994–1002, https://doi.org/10.1016/j.jallcom.2018.07.199.

[31] C. López-Pernía, A. Morales-Rodríguez, Á. Gallardo-López, R. Poyato, Enhancing the electrical conductivity of in-situ reduced graphene oxide-zirconia composites through the control of the processing routine, Ceram. Int. 47 (2021) 9382–9391, https://doi.org/10.1016/j.ceramint.2020.12.069.

[32] H.D. Carlton, J.W. Elmer, D.C. Freeman, R.D. Schaeffer, O. Derkach, G.F. Gallegos, Laser notching ceramics for reliable fracture toughness testing, J. Eur. Ceram. Soc. 36 (2016) 227–234, https://doi.org/10.1016/j.jeurceramsoc.2015.08.021.

[33] Y. Torres, R. Bermejo, L. Llanes, M. Anglada, Influence of notch radius and R-curve behaviour on the fracture toughness evaluation of WC–Co cemented carbides, Eng. Fract. Mech. 75 (2008) 4422–4430, https://doi.org/10.1016/j.engfracmech.2008.04.017.

[34] M. Turon-Vinas, J. Morillas, P. Moreno, M. Anglada, Evaluation of damage in front of starting notches induced by ultra-short pulsed laser ablation for the determination of fracture toughness in zirconia, J. Eur. Ceram. Soc. 37 (2017) 5127–5131, https://doi.org/10.1016/j.jeurceramsoc.2017.07.006.

[35] Á. Gallardo-López, J. Castillo-Seoane, C. Muñoz-Ferreiro, C. López-Pernía, A. Morales-Rodríguez, R. Poyato, Flexure strength and fracture propagation in zirconia ceramic composites with exfoliated graphene nanoplatelets, Ceramics 3 (2020) 78–91, https://doi.org/10.3390/ceramics3010009.

[36] C.M. Phillippi, K.S. Mazdiyasni, Infrared and Raman spectra of zirconia polymorphs, J. Am. Ceram. Soc. 54 (1971) 254–258, https://doi.org/10.1111/j.1151-2916.1971.tb12283.x.

[37] S. Giese, F. Kern, C.A. Macauley, S. Neumeier, M. Göken, Fracture resistance of yttria stabilized zirconia manufactured from stabilizer-coated nanopowder by micro cantilever bending tests, J. Eur. Ceram. Soc. 39 (2019) 3830–3836, https://doi.org/10.1016/j.jeurceramsoc.2019.05.006.

[38] A. International, ASTM C1421-10, Standard Test Methods for Determination of Fracture Toughness of Advanced Ceramics at Ambient Temperature, ASTM International, West Conshohocken, 2010, https://doi.org/10.1520/C1421-10.

[39] M.E. Ebrahimi, J. Chevalier, G. Fantozzi, R-curve evaluation and bridging stress determination in alumina by compliance analysis, J. Eur. Ceram. Soc. 23 (2003) 943–949, https://doi.org/10.1016/S0955-2219(02)00230-3.

[40] S. Rani, M. Kumar, S. Sharma, D. Kumar, Role of graphene in structural transformation of zirconium oxide, J. Sol-Gel Sci. Technol. 71 (2014) 470–476, https://doi.org/10.1007/s10971-014-3401-x.

[41] A. Nieto, L. Huang, Y.H. Han, J.M. Schoenung, Sintering behavior of spark plasma sintered alumina with graphene nanoplatelet reinforcement, Ceram. Int. 41 (2015) 5926–5936, https://doi.org/10.1016/j.ceramint.2015.01.027.

[42] S.-M.M. Kwon, S.-J.J. Lee, I.-J.J. Shon, Enhanced properties of nanostructured ZrO2-graphene composites rapidly sintered via high-frequency induction heating, Ceram. Int. 41 (2014) 835–842, https://doi.org/10.1016/j.ceramint.2014.08.042.

[43] B. Yazdani, H. Porwal, Y. Xia, H. Yan, M.J. Reece, Y. Zhu, Role of synthesis method on microstructure and mechanical properties of graphene/carbon nanotube toughened Al2O3 nanocomposites, Ceram. Int. 41 (2015) 9813–9822, https://doi.org/10.1016/j.ceramint.2015.04.054.

[44] H. Seiner, C. Ramirez, M. Koller, P. Sedlák, M. Landa, P. Miranzo, M. Belmonte, M.I. Osendi, Elastic properties of silicon nitride ceramics reinforced with graphene nanofillers, Mater. Des. 87 (2015) 675–680, https://doi.org/10.1016/j.matdes.2015.08.044.

[45] H. Porwal, S. Grasso, M.J. Reece, Review of graphene–ceramic matrix composites, Adv. Appl. Ceram. 112 (2013) 443–454, https://doi.org/10.1179/174367613X13764308970581.

[46] C. Lee, X. Wei, J.W. Kysar, J. Hone, Measurement of the elastic properties and intrinsic strength of monolayer graphene, Science 321 (2008) 385–388, https://doi.org/10.1126/science.1157996.

[47] C. Gómez-Navarro, M. Burghard, K. Kern, Elastic properties of chemically derived single graphene sheets, Nano Lett. 8 (2008) 2045–2049, https://doi.org/10.1021/nl801384y.

[48] Y. Zhang, C. Pan, Measurements of mechanical properties and number of layers of graphene from nano-indentation, Diam. Relat. Mater. 24 (2012) 1–5, https://doi.org/10.1016/j.diamond.2012.01.033.

[49] J. Eichler, J. Rödel, U. Eisele, M. Hoffman, Effect of grain size on mechanical properties of submicrometer 3Y-TZP: fracture strength and hydrothermal degradation, J. Am. Ceram. Soc. 90 (2007) 2830–2836, https://doi.org/10.1111/j.1551-2916.2007.01643.x.

[50] J. Wang, M. Rainforth, R. Stevens, The grain size dependence of the mechanical properties in TZP ceramics, in: Zirconia'88, Springer, Netherlands, Dordrecht, 1989, pp. 337–366, https://doi.org/10.1007/978-94-009-1139-0_31.

[51] J. Eichler, M. Hoffman, U. Eisele, J. Rödel, R-curve behaviour of 2Y-TZP with submicron grain size, J. Eur. Ceram. Soc. 26 (2006) 3575–3582, https://doi.org/10.1016/j.jeurceramsoc.2005.11.012.

[52] J. Chevalier, C. Olagnon, G. Fantozzi, Subcritical crack propagation in 3Y-TZP ceramics: static and cyclic fatigue, J. Am. Ceram. Soc. 82 (2004) 3129–3138, https://doi.org/10.1111/j.1151-2916.1999.tb02213.x.

[53] M. Li, Z. Feng, P. Ying, Q. Xin, C. Li, Phase transformation in the surface region of zirconia and doped zirconia detected by UV Raman spectroscopy, Phys. Chem. Chem. Phys. 5 (2003) 5326–5332, https://doi.org/10.1039/b310284j.

[54] D. Casellas, J. Alcalá, L. Llanes, M. Anglada, Fracture variability and R-curve behavior in yttria-stabilized zirconia ceramics, J. Mater. Sci. 36 (2001) 3011–3025, https://doi.org/10.1023/A:1017923008382.

[55] I.A. Ovid'ko, Micromechanics of fracturing in nanoceramics, Philos. Trans. R. Soc. A Math. Phys. Eng. Sci. 373 (2015) 20140129, https://doi.org/10.1098/rsta.2014.0129.

[56] D.-T. Vu, Y.-H. Han, F. Chen, D. Jin, J.M. Schoenung, D.-Y. Lee, Graphene nano-platelets reinforced ZrO2 consolidated by spark plasma sintering, Sci. Adv. Mater. 8 (2016) 312–317, https://doi.org/10.1166/sam.2016.2485.

[57] C. Ramirez, M.I. Osendi, Toughening in ceramics containing graphene fillers, Ceram. Int. 40 (2014) 11187–11192, https://doi.org/10.1016/j.ceramint.2014.03.150.

[58] M.E. Ebrahimi, J. Chevalier, G. Fantozzi, Slow crack-growth behavior of alumina ceramics, J. Mater. Res. 15 (2000) 142–147, https://doi.org/10.1557/JMR.2000.0024.